Squish Jamming

Samuel Poincloux[1, *] and Kazumasa A. Takeuchi[1, 2, †]

[1]*Department of Physics, The University of Tokyo, 7-3-1 Hongo, Bunkyo-ku, Tokyo 113-0033, Japan*
[2]*Institute for Physics of Intelligence, The University of Tokyo, 7-3-1 Hongo, Bunkyo-ku, Tokyo 113-0033, Japan*
(Dated: April 16, 2024)

A wide range of disordered materials, from biological to geological assemblies, feature discrete elements undergoing large shape changes. How significant geometrical variations at the microscopic scale affect the response of the assembly, in particular rigidity transitions, is an ongoing challenge in soft matter physics. However, the lack of a model granular-like experimental system featuring large and versatile particle deformability impedes advances. Here, we explore the oscillatory shear response of a sponge-like granular assembly composed of highly compressible elastic rings. We highlight a progressive rigidity transition, switching from a fluid-like to a solid-like response by increasing density or decreasing shear amplitude. The rearranging fluid state consists of crystal clusters separated by melted regions; in contrast, the solid state remains amorphous and absorbs all imposed shear elastically. We rationalise this transition by uncovering an effective, attractive shear force between rings that emerges from a friction-geometry interplay. If friction is sufficiently high compared to shear, the extent of the contacts between rings, captured analytically by elementary geometry, controls the rigidity transition.

Particulate assemblies, such as granular media, can switch their mechanical behaviour between a solid and a fluid-like response depending on their density, applied stress or interactions. This solid-fluid transition is of tremendous importance across length scales and disciplines, with the elemental particles varying in size, shape, and stiffness. Such jamming or yielding transitions are, for instance, underlying the onset of geological flows [1], the transport and clogging in industrial food processing [2], and are at the heart of numerous biological processes [3].

For rigid particles without internal degrees of freedom, the rigidity transition is mainly controlled by the average number of constraints imposed by the number of neighbours [4], including for non-spherical particles [5]. Even when particles are softer and can moderately deform their shape upon contact, such as emulsions or foams, the number of contacts remains an essential factor [6–8]. However, particle deformations may reach up to the order of the particle size for a broader class of materials, from biological tissues to porous soils. By adapting their shape to external constraints, such *squishy* particles [9] acquire additional degrees of freedom, potentially affecting the fluid-solid transition ingredients.

Recent works highlight the role of shape and deformability in the jamming transition of highly deformable particles, both in thermal [10, 11] and athermal [12–14] assemblies. Dedicated tools have also been developed to quantify the large shape changes that cells undergo while embedded in a deforming tissue [15]. The shape of the cells in epithelial tissues is one of the essential parameters governing a rigidity transition [16–18]. In geological flows, the shape of constitutive particles undergoes significant changes primarily via breaking [19], which in turn have a critical effect on the rheology [20] and jamming transition [1, 21]. With very soft grains that do not

break, compaction far above jamming highlights that not only the coordination number increases with compaction, but also the size of the contacts [22, 23].

Despite these recent advances, a clear picture of how extreme deformability affects the fluid-solid transition is still lacking. It is an ongoing challenge in soft matter physics and related fields [24]. Although advanced numerical methods, such as the vertex model [18], the material point method [25] and phase field approach [26, 27], have been used, numerical investigations remain incredibly challenging owing to the non-linear couplings between geometry and interactions at the local scale, and a large number of elements. As such, a simple experimental model featuring large deformation at the grain scale would be essential to explore this question. One may leverage the recent advances in granular metamaterials [28] and metafluids [29], whose properties are governed by geometrical non-linearities at the particle scale, to control grains compressibility.

Here, we introduce assemblies of compressible elastic rings as an experimental model to explore the role of large grain deformations in the rheology of disordered media. Via oscillatory shear experiments, we highlight a solid-fluid transition controlled by the shear amplitude and the density. While the transition is characterised by the absence or presence of structural rearrangements, compression-induced large geometrical deformations help the assembly absorb shear without rearranging in the solid phase. Finally, we argue that this transition is mainly driven by the size of the frictional contacts between the compressed rings via effective adhesive interactions under shear, which stem from the interplay between geometrical deformations and friction.

Fluid-solid transition in a sheared assembly of compressible rings

We consider a two-dimensional assembly of frictional, elastic, and ring-shaped grains (see Fig. 1**a** and Supplementary Video 1). The assembly is compressed into an imposed area and sheared by oscillatory displacement of the top boundary as shown in the setup schematic in Fig. 1**a**. The rings are all identical with a thickness $t = 1.5$ mm, radius $r = 3.3$ mm and height $h = 10$ mm. Rings are fabricated via moulding of polymerising liquid silicone (see Methods and Supplementary Fig. 1), then coated with talc powder to avoid adhesion and ensure dry frictional interactions. The compression response of the rings to a loading-unloading cycle (Fig. 1**b**) attests to a perfect elasticity with no remaining permanent deformations and high reproducibility, and is well recovered by the finite element method (FEM) (see Methods for details). In addition, the onset of the compression response features a small stiffness decrease (Fig. 1**c**). Deformed rings being slightly softer, a compressed assembly of such rings develops heterogeneous deformations as shown in the top view displayed in Fig. 1**d** (see also Supplementary Video 1). This heterogeneous deformation upon compression is reminiscent of the mechanics of cellular materials [30–32], including solid foams [33], with the critical difference that here the unit cells do not adhere each other and can therefore rearrange.

The assembly's response to shear is explored by systematically varying the shear amplitude γ_0 and the density of rings Φ. The oscillatory shear γ is imposed at a fixed maximum shear rate of $\dot{\gamma}_0 = 1.33 \times 10^{-2}\,\text{s}^{-1}$, low enough to ensure a quasi-static regime where inertial or vibrational effects are negligible. The density is adjusted by varying the number of rings in the shear cell and quantified by $\Phi = N\pi r_h^2/A$ with $r_h = r + t/2$ the external radius of the rings, N the number of rings and A the area of the shear cell. This is the density that would correspond to the undeformed area of the rings, and we focus on the regime above the hexagonal packing density $\Phi_h = \frac{\pi}{2\sqrt{3}} \approx 0.91$. Initialisation is made by dispersing the rings in the cell area and then manually lowering and fixing the top arm at the desired height. The ring assembly is, therefore, initially in a mechanically quenched state. An acrylic plate on top of the assembly holds the rings in 2D, preventing out-of-plane buckling.

The mechanical response to shear is probed locally via image analysis and globally via a force sensor. Pictures from an overhanging camera are taken regularly during the cycles, such that the position, shape and neighbours of each ring are identified and tracked all along the shear cycles (Fig. 1**e**; see also Methods and Supplementary Video 2). A force sensor, placed between the driving screw and the top arm, records the force F_X necessary to shear the assembly. The shear force F_X for $\Phi = 1.0$

and all investigated shear amplitudes is shown in Fig. 1**f**. Unless stated otherwise, the presented measures represent the system in the steady state (see Supplementary Table 1 for the cycles used in the analysis). The high reproducibility of the shear response in Fig. 1**f** testifies that the assembly indeed reached a steady state.

We then assess whether the ring assembly responds more in a solid-like (jammed) or fluid-like (yielded) fashion. To assess this response, a classic measure for particulate systems under oscillatory loading is the irreversible displacement of the particles between two consecutive cycles [34–39]. We define $\Delta u(i, c)$ as the norm of the irreversible displacement of ring i occurring between the start and end of cycle c. In Fig. 1**d**, rings are coloured by their value of $\log(\Delta u/r)$ and the associated irreversible displacement is drawn with a red arrow (magnified by a factor 4). Even at such a high density, irreversible displacements occur but are highly heterogeneous, with values spanning orders of magnitude within the assembly. To explore how the irreversibility depends on the density and shear amplitude, for each parameter pair (Φ, γ_0) considered, we compute $\langle\Delta u\rangle$, the averaged irreversible displacement over all tracked rings in the steady state. The resulting map is shown in Fig. 1**g**. Two zones can be identified: a fluid-like regime with significant irreversibility, which smoothly transitions to a solid-like zone with barely any irreversible displacement, by increasing density or decreasing shear (see also non-affine trajectories in Supplementary Video 3).

The transition between the fluid-like and solid-like features is observed not only in the rings' local movement but also via the global mechanical response. From the shear response $F_X(\gamma)$ of the whole assembly, we compute for each cycle the first harmonic of the storage and loss moduli, G' and G'', respectively [40] (see separated map of G'' and G' in Extended Data Fig. 1). Identifying when the ratio G''/G' is greater than 1 is a standard method to evaluate if the assembly yields or remains essentially solid [41]. The map of $\log(\langle G''\rangle / \langle G'\rangle)$ shown in Fig. 1**h**, with $\langle G''\rangle, \langle G'\rangle$ the moduli averaged over the cycles in the steady state, recovers qualitatively the solid- and fluid-like regions identified above from the irreversible displacements (Fig. 1**g**). Indeed, the region with high irreversible displacements coincides with a loss modulus significantly larger than the storage one and inversely for the dominantly reversible region.

Exploring the mechanical response to shear at very high density and shear amplitude, we identify a progressive jamming transition of the ring assembly by either reducing the shear amplitude or increasing the density. To understand the driving factors of this transition, we first quantify the structural properties of the assembly.
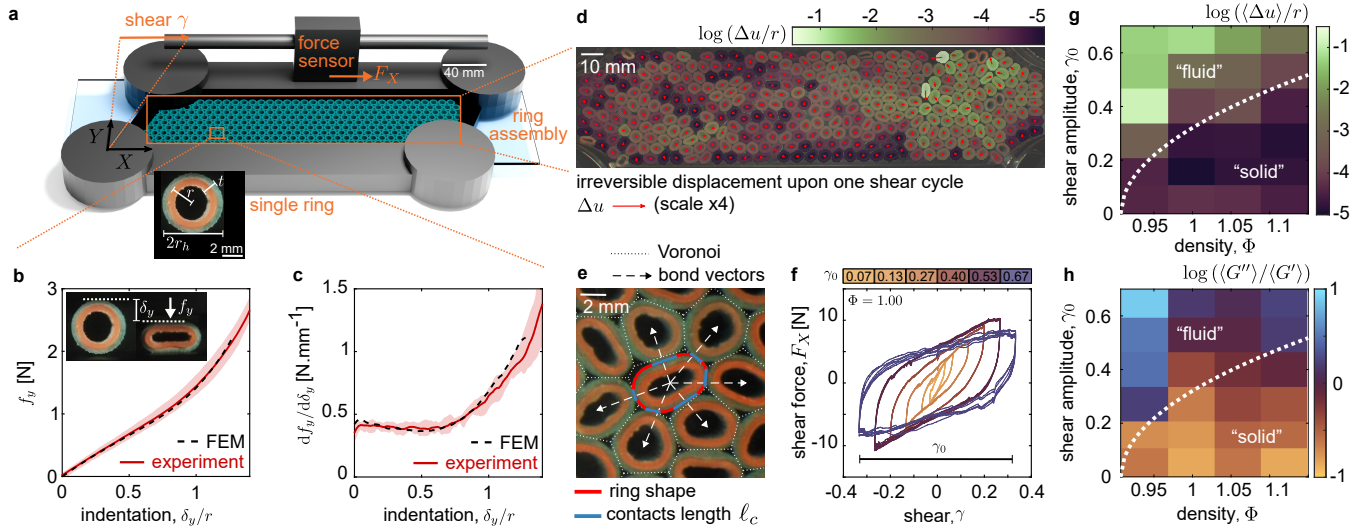
Fig. 1 | Fluid-solid transition under oscillatory shear of an assembly of compressible rings. a, Schematic of the experimental setup. A ring assembly is confined within a 2D cell with a fixed area. Oscillatory shear $\gamma = (\gamma_0/2)\sin\left(2\dot{\gamma}_0 t/\gamma_0\right)$ is applied to the assembly via lateral motion of the top arm while the bottom one is fixed. Both top and bottom arms are decorated with half-solid disks of the same dimension as the rings to transmit shear. A transparent acrylic plate placed on top keeps the rings in the plane. **b**, Experimental and simulated (FEM) indentation response $f_y(\delta_y)$, and **c**, associated stiffness $\frac{\mathrm{d}f_y}{\mathrm{d}\delta_y}$ of a single ring compressed between two flat plates. The experimental curve is the averaged response over five different rings from the assembly; upon loading and unloading, the shaded area shows the minimal and maximal values reached by the rings during the compression cycle. The corresponding FEM response is made via a 3D simulation of the neo-Hookean material model with Young's modulus $E = 1\,\mathrm{MPa}$ and Poisson's ratio $\nu = 0.45$, reproducing the ring and indentation geometry. The experiments and FEM, which agree quantitatively, feature a slight softening upon indentation, leading to solid foam-like deformation heterogeneities upon compression of the ring assembly. **d**, Top view of the ring assembly ($\Phi = 1.04$ and $\gamma_0 = 0.53$) and representative of the pictures used for image analysis. Here, each tracked ring is coloured over its detected area by the value of its irreversible displacement $\log(\Delta u/r)$. The corresponding displacement is shown by a red arrow (up-scaled by a factor 4). **e**, For each ring, we measure via image analysis its position (geometric centre), shape, neighbours, and extent of each contact (length of the blue segments). We define two neighbourhood types: Voronoi neighbours share a common edge in the Voronoi tessellation, and touching neighbours are in contact with a finite contact extent ℓ_c. The thin orange silicone layer is applied in the inner part of the ring to help with detection and further imaging processes. See also Supplementary Video 2. **f**, Shear response $F_X(\gamma)$ of the assembly for $\Phi = 1.00$ and for shear amplitude γ_0 ranging from 0.07 to 0.7. Six cycles in the steady state are displayed for each γ_0. **g**, Intensity of the averaged irreversible displacement $\log(\langle\Delta u\rangle/r)$ for varying density Φ and shear amplitude γ_0. The average is calculated over all tracked rings and in the steady state. **h**, Map of the ratio between the loss and storage moduli of the assembly, computed from the shear response $F_x(\gamma)$ and averaged over the cycles in the steady state. The corresponding $F_x(\gamma)$ for $\Phi = 1.00$ are shown in **f**, each coloured by its corresponding value of $\log(\langle G''\rangle/\langle G'\rangle)$. In **g**,**h**, and subsequent maps, the white dotted line is a geometric prediction introduced thereafter (Eq. (1)), but now serves as a reference to help compare the maps and identify solid and fluid regions.

A partially crystallised fluid and an amorphous solid

The presence or absence of irreversible displacements upon cyclic shear in the steady state highlights that ring rearrangements and associated structural deformations play a crucial role in the mechanical response of the assembly [42, 43]. We then measure the structural differences between the solid and fluid regions and how they evolve from their initial quenched state. With all rings having the same size, the configuration with the highest density and minimal shape deformation (and hence minimum elastic energy) is the hexagonal packing. We thus use the hexagonal bond orientational order Ψ_6 as the structural indicator of the assembly [44]. For each ring j, the hexagonal order is computed by $\Psi_6(j) =$

$(1/n_j)|\sum_{k=1}^{n_j} \mathrm{e}^{6\mathrm{i}\alpha_{jk}}|$ with n_j the number of Voronoi neighbours and α_{jk} the angle between the line passing through the centre of the two rings and the x axis (the direction of the shear). The value of Ψ_6 is 1 for a ring in a perfect hexagonal lattice and continuously decreases to 0 as the structure deviates from the hexagonal one.

As the assembly accumulates shear cycles, we compare in Fig. 2 (see also Supplementary Video 4) the structural evolution of configurations for two cases located near the border between the jammed and yielded regions, with each case positioned on the opposite side of the border. After mechanical quenching, both configurations start in an amorphous state with a flat probability distribution $P(\Psi_6)$, but their evolution with cycling strongly differ. In the yielded region, for $(\gamma_0, \Phi) = (0.4, 1.00)$ shown in
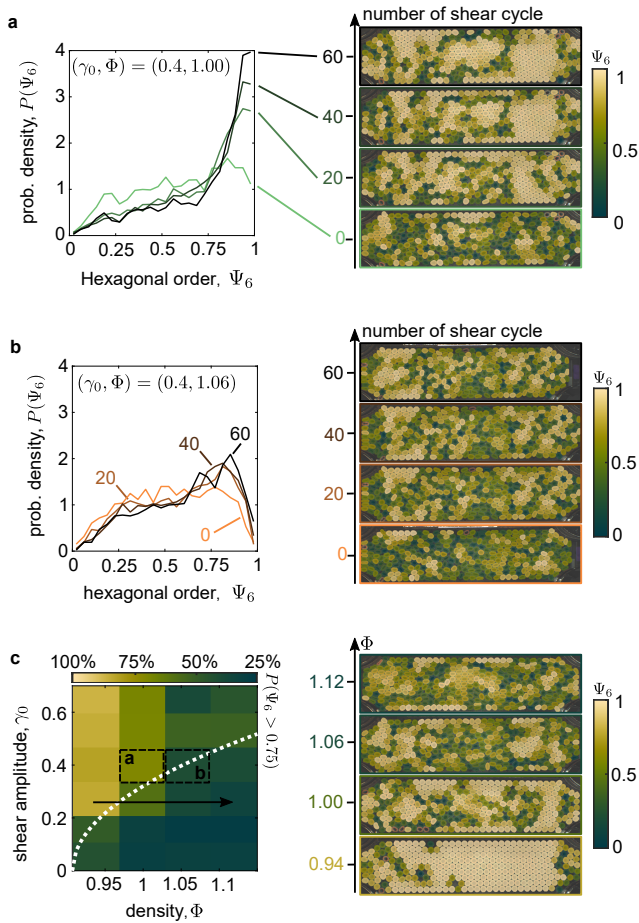
Fig. 2 | Crystallising fluid and amorphous solid. a,
Left, probability density profiles of the hexagonal bond
orientational order Ψ_6 for an assembly at
$(\gamma_0, \Phi) = (0.4, 1.00)$ in the yielded region. The profiles are
shown for the assembly before shear and after 20, 40 and 60
shear cycles. Right, corresponding snapshots of the assembly
after cycling, where each ring is coloured by its Ψ_6 value.
The assembly shows a progressive growth of crystalline
regions separated by melted ones. **b,** Same quantities as in **a**
but for an assembly with higher density and same shear
amplitude, $(\gamma_0, \Phi) = (0.4, 1.04)$, now located in the jammed
region. Here, no significant structural changes are observed,
and despite high shear, the assembly remains amorphous.
See also Supplementary Video 4. **c,** Map of the proportion of
rings belonging to crystal clusters (with $\Psi_6 > 0.75$) in the
steady state. The corresponding snapshots of the assemblies
in their steady states, with the rings coloured by their Ψ_6
values, are shown on the right for $\gamma_0 = 0.25$ and all
investigated densities. See also Supplementary Video 5 for
the time evolution of Ψ_6.

Fig. 2**a**, cycling induces drastic structural changes with
the progressive growth of distinct crystal clusters. The
probability density increases close to $\Psi_6 = 1$ while it
decreases for low values. In contrast, for larger densi-
ties within the jammed region (with $(\gamma_0, \Phi) = (0.4, 1.06)$
shown in Fig. 2**b**), no significant structural changes occur

upon cycling, and the assembly remains in an amorphous
phase. We then measure the crystallised portion of the
assembly, or proportion of rings having $\Psi_6 > 0.75$, in the
steady state over the parameter space (Fig. 2**c**). All the
assemblies in the solid region feature almost no structural
changes and remain amorphous, while the proportion of
the crystal clusters decreases with increasing density in
the fluid region (Fig. 2**c**; see also Supplementary Video 5).
Rearranging rings within a given surface area tend to
crystallise to reduce their overall elastic energy, as the
hexagonal packing is the most compact structure with-
out shape deformations. However, the growth of crystal
clusters is limited by the presence of rings deformed by
compression, which necessarily exist for high densities
and prevent crystallisation.

The structure of the ring assembly in its steady state
differs drastically between the yielded and jammed re-
gions. The fluid-like region is characterised by hexagonal
crystal clusters separated by a melted, disordered phase.
This partial crystallisation is typical of granular media
under sufficient shear where reorganisations lead to struc-
tural changes [45–48]. Even if essentially crystallised,
the yielded phase still displays a fluid-like mechanical
response with irreversible displacements (Fig. 1**g,h**). In
contrast, no crystallisation occurs in the jammed region,
where the assembly remains amorphous almost without
rearrangements. Even under high shear, the rings stick
together to keep the same structure. In the following,
we delve into the dynamics during shear cycles to inves-
tigate the interplay between structural and geometrical
deformations of the rings.

Large geometrical deformations absorb shear and hinder rearrangements

We now focus on the deformation of rings during shear
cycles to understand how yielded and jammed regions
respond to shear. The geometry, of the rings is quanti-
fied by the shape index $q = (\text{ring perimeter})/\sqrt{\text{ring area}}$,
a classic quantity used in highly deformable assemblies
like epithelial tissues [16, 17] to assess how far a convex
shape is from a circle. The shape index takes the value
$q = 2\sqrt{\pi} \approx 3.54$ for a perfect circle and increases when
the ring gets deformed. As the rings are slender objects,
they deform mostly by flexion rather than stretching.
Thus, q is mainly increased by reducing the area while
the perimeter is almost unchanged. This contrasts with
emulsions or tissues where most deformations originate
from a change in perimeter and not the area [7, 27]. The
perimeter and area of the rings are obtained via image
analysis, and a Fourier decomposition is used to smooth
the pixelated shape and reduce the shape to a few de-
scriptors [27]. The resulting measure of q during a shear
cycle is shown in Fig. 3**a** for one ring within an assembly
with parameters $(\gamma_0, \Phi) = (0.4, 1.00)$. For each cycle c
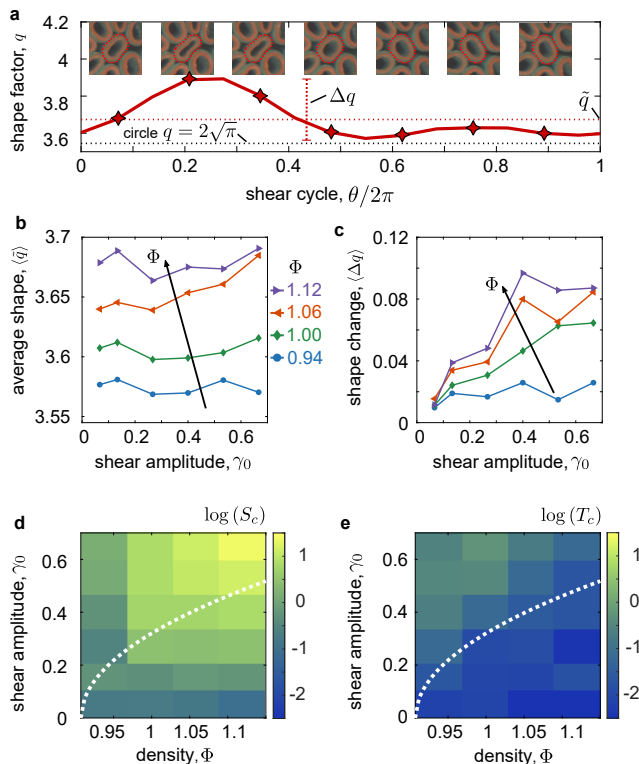
Fig. 3 | Competition between geometrical and structural deformations. a, The geometrical deformation of the rings is quantified by the shape index q. The evolution of q within a cycle is shown for one ring in a $(\gamma_0, \Phi) = (0.4, 1.00)$ assembly. Each marker goes with an associated ring snapshot. We extract $\tilde{q}$ and Δq, the average and amplitude variation from the shape trajectory. **b,c**, Average shape of the assembly $\tilde{q}$ and shape variation Δq as a function of shear amplitude for each density. The values are averaged over all tracked rings in the steady state. **d,e**, Map of the geometrical S_c and topological T_c strains of the assembly. The total strains here are the cumulative sums of the norm of the frame-to-frame strains estimated over the whole assembly and in the steady state.

and tracked ring, we define two quantities from the shape trajectory: the average deformation $\tilde{q} = \langle q \rangle_{\text{cycle}}$ and the geometrical fluctuation $\Delta q = \max(q)_{\text{cycle}} - \min(q)_{\text{cycle}}$.

In the steady state, the mean shape index and fluctuation are then averaged over all tracked rings, and their dependence on shear is compared for each density Fig. 3**b,c**. As expected, the average geometrical deformation $\tilde{q}$ increases steadily with the density Fig. 3**b**. For all densities, increasing shear amplitude drives significant shape fluctuations during shear cycles, and the higher the density, the more pronounced the geometrical changes (Fig. 3**c**). Thus, a higher density contributes, in addition to naturally increasing the average geometrical deformation, to promoting shape changes for a given imposed shear. Ring assemblies, therefore, use their compressibility and shape-changing abilities to absorb imposed exter-

nal shear, and they do so more efficiently as the density increases.

To grasp the combined role of geometrical changes and structural rearrangements leading to jammed or yielded assemblies, we quantify these two aspects by dedicated strains derived for epithelial tissue deformations [15]. For each ring and between each time frame, we track the bond vectors between touching neighbours (Fig. 1**e** and Supplementary Video 6). The geometrical strain S^* is derived from the change in bond length and orientation and quantifies changes in size and shape within the assembly. In contrast, the topological strain T^*, based on the appearance or creation of bonds due to rearrangements, captures the change in the topology of the contact network and then quantifies the structural deformations of the assembly. More details on these quantities are given in the Methods, and their step-by-step derivation is in the Appendix of Ref.[15]. The strains S^* and T^* are computed between each time frame and for the whole assembly. Their norm is then summed over all the cycles in the steady states to obtain the quantities $S_c = \int_t \|S^*\| \mathrm{d}t$ and $T_c = \int_t \|T^*\| \mathrm{d}t$ shown in Fig. 3**d,e**. From the map of $\log S_c$ over (γ_0, Φ) in Fig. 3**d**, we observe that geometrical changes increase significantly with both shear amplitude and density as observed in Fig. 3**c**. By contrast, the map of $\log T_c$ in Fig. 3**e** shows that structural deformations, while increasing with shear amplitude, are diminished by higher densities. As a result, the region where changes in the topology of the contact network are significant coincides with the fluid region identified in Fig. 1**g,h**. Yet, the geometrical deformations vary regardless of the fluid or solid regions.

In contrast to confluent bi-dimensional active cell models where more significant deformations lead to yielding [18], here, deforming the assembly by increasing the density fosters jamming by absorbing shear and hindering structural rearrangements. We then investigate the ring-ring interactions to understand the mechanisms under which large shape deformations impede structural ones.

Geometry and friction concur to generate effective shear adhesion between rings.

We introduce a microscopic ersatz comprising two half-rings sequentially compressed and sheared to measure the interaction between rings. Then, we will link the sign of the shear force, which would promote or prevent structural rearrangements, to the assembly's fluid-solid transition.

We measure, via FEM and experiments, the shear response of two clamped rings compressed by an amount δ_y (Fig. 4**a** and Supplementary Video 7). With FEM, we systematically vary the frictional interaction via the friction coefficient μ of the sheared interfaces (Fig. 4**b**) and the compression δ_y between the rings (Fig. 4**c**). Experi-
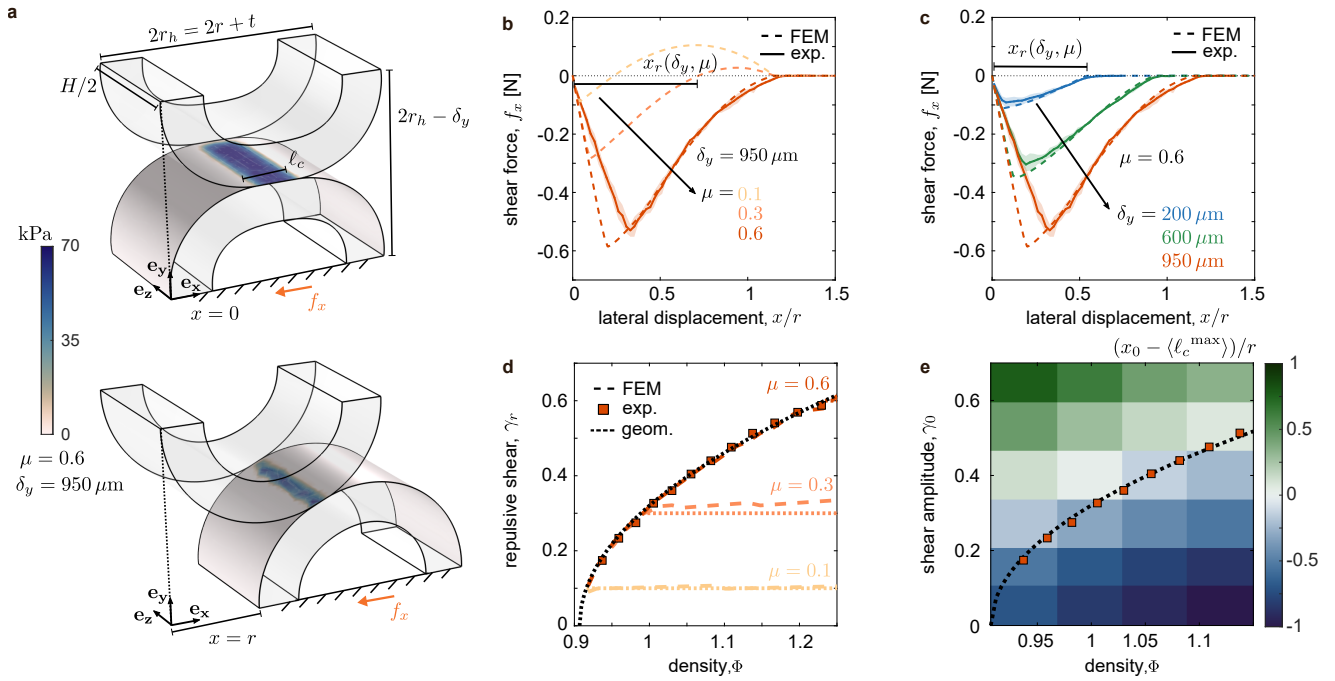
Fig. 4 | Friction and geometrical deformations produce an effective shear adhesion between the rings. a, Ring-ring interaction experiments and FEM simulations. Two facing half-rings are compressed over a distance δ_y and then sheared laterally until they lose contact. Displayed are two FEM snapshots showing the contact pressure between the rings after compression, before (top) and after (bottom) a lateral shear displacement of $x = r$. See also Supplementary Video 7. **b,c**, The resulting shear interaction force f_x is measured as a function of the lateral displacement x. Negative (positive) values indicate an attractive (repulsive) force between the rings. Experimental responses are averaged over 3 distinct pairs, and shaded areas represent max and min values obtained from the different pairs. Panel **b** shows the shear response $f_x(x)$ for $\delta_y = 950 \, \mu$m and the friction coefficient $\mu = 0.1, 0.3, 0.6$ varied in the FEM. The experimental response matches that of FEM for $\mu = 0.6$. Panel **c** shows the shear response $f_x(x)$ for $\mu = 0.6$, for increasing confinement $\delta_y = 200, 600, 950 \, \mu$m. In this high friction regime, f_x remains negative until the separation of the rings. We measure $x_r(\delta_x, \mu)$, the displacement needed to switch from attractive ($f_x < 0$) to repulsive ($f_x > 0$) shear interactions. **d**, Experimental measure of the attractive-repulsive threshold shear $\gamma_r(\Phi)$, obtained by translating local quantities (δ_y, x_r) to global ones (Φ, γ_r), together with results from FEM (dashed lines) and the geometrical predictions (dotted lines) for $\mu = 0.1, 0.3, 0.6$. This curve $\gamma_r(\Phi)$ for $\mu = 0.6$ is the one drawn in the phase diagrams shown so far (e.g., Fig. 1**g,h**), marking the fluid-solid transition of the assembly (fluid-like for $\gamma_0 > \gamma_r$ and solid-like otherwise). **e**, (Φ, γ_0) map of the difference between the imposed shear displacement x_0 and the measured maximal contact size $\langle \ell_c^{\max} \rangle$, averaged over all tracked rings in the steady state. The geometrical prediction and local measurements of the attractive-repulsive threshold γ_r correspond to the region where $y_0 \approx \langle \ell_c^{\max} \rangle$. In this high friction and large geometrical deformations limit, the extent of the contacts ℓ_c mainly controls the jamming transition.

mentally, we test rings taken from the assembly by applying the same compression values as in FEM. We find the best agreement between the experiments and the FEM for $\mu = 0.6$, constituting a measure of the experimental friction coefficient. In the absence of friction, the shear force f_x is instantly positive (repulsive) as elastic deformations push the rings away from each other. With friction, however, f_x starts negative (attractive) and a finite lateral displacement $x_r(\delta_y, \mu)$ is required to make it repulsive ($f_x > 0$). The synergy of geometrical deformation and friction thus produces an attractive interaction, or effective adhesion, between the rings until sufficient shear is applied. The role of shape change to generate an effective adhesion under shear is reminiscent of the rheology of cohesive granular media [49], where the low stiffness of the grains also participates in producing a

higher effective adhesion. We argue next that the presence or absence of this effective adhesion under shear is at the root of the assembly's fluid or solid macroscopic response.

We now give a geometrical prediction of the finite lateral displacement x_r necessary to switch the shear interactions force from attractive to repulsive, i.e., $f_x(x_r) = 0$. This distance is a function of the initial compression δ_y and the friction between the rings, μ. Two cases emerge in the way $x_r(\delta_y, \mu)$ is determined. In the first case, the rings remain in contact when f_x switches from negative to positive (e.g., Fig. 4**b** for $\mu = 0.1$ and 0.3). In this case, assuming Amontons-Coulomb frictional properties and reducing the contacting interfaces to a point, one can directly link the sign of the shear force f_x to the lateral displacement and obtain $x_r(\delta_y, \mu) = \mu(2r_h - \delta_y)$. By con-

trast, in the second case where f_x remains negative until the rings are fully separated (e.g., Fig. 4**c**), x_r is given by the extent of the initial overlap between the rings: $x_r(\delta_y, \mu) = 2r_h\sqrt{1 - (1 - \delta_y/(2r_h))^2}$. Now that we have a prediction for the microscopic ring-ring interactions, we must translate the compression δ_y and local lateral displacement x to the global variable density Φ and shear γ. Assuming an hexagonal structure of density Φ_h, an isotropic local overlap δ_y directly translates into a density by $\Phi(\delta_y) = \Phi_h/(1 - \delta_y/(2r_h))^2$. For the shear γ, too, by using its local counterpart, i.e., the local shear imposed between the two half rings, we obtain $\gamma = x/(2r_h - \delta_y)$. Schematics of the underlying geometrical predictions are shown in Extended Data Fig. 2. By combining the expressions of $x_r(\delta_y, \mu)$ with the expressions of $\Phi(\delta_y)$ and $\gamma(y, \delta_y)$, we can finally express the repulsive shear γ_r at which the interactions become repulsive as a function of global variables (γ, Φ), as follows:

$$\gamma_r(\Phi, \mu) = \begin{cases} \sqrt{\dfrac{\Phi}{\Phi_h} - 1} & \text{if } \gamma_r < \mu \\ \mu & \text{if } \gamma_r \geq \mu \end{cases} \quad (1)$$

In Fig. 4**d**, we compare γ_r from the prediction against FEM and experimental measurements and find a perfect match. In the high friction case ($\gamma_r < \mu$), the threshold $\gamma_r(\Phi)$ is simply set by the extent of contacts, yielding $\gamma_r(\Phi) = \sqrt{\Phi/\Phi_h - 1}$. Experimentally, the explored density range and the estimated friction coefficient $\mu \approx 0.6$ are such that we remain in this high friction limit. In soft spheres without shape changes, the jamming transition also features a scaling between yielding and density [50] but occurs at a much lower density and with a different scaling.

With repulsive interactions between rings, we expect structural rearrangements to be promoted and, inversely, hindered if interactions are attractive and act as an effective adhesive force. The shear γ_r can then be viewed as a yield shear, where rearrangements leading to fluid-like response are expected for $\gamma_0 > \gamma_r$, and a solid-like jammed assembly for $\gamma_0 < \gamma_r$. Indeed, the line drawn by the geometric prediction of Eq. (1) qualitatively separates the fluid and solid-like regions in the (Φ, γ_0) parameter space (Fig. 1**g,h**), which also accompany significant changes of the contact network topology (Fig. 3**e**). This geometric boundary $\gamma_r(\Phi) = \sqrt{\Phi/\Phi_h - 1}$ is set by the extent of the contact between rings, which increases with density. To verify that the contact extent is a major factor controlling the fluid-solid transition, we measure $\ell_c^{\max}$, the largest contact length among all touching neighbours, for each ring and at each time step. We then compute the difference between the equivalent local lateral displacement amplitude $x_0 = \gamma_0(2r_h - \delta_y) = \gamma_0 2r_h\sqrt{\Phi_h/\Phi}$ and $\langle \ell_c^{\max} \rangle$, averaged in the steady state (Fig. 4**e**). The geometrical prediction of γ_r matches with the region where $x_0 \approx \langle \ell_c^{\max} \rangle$. The fluid-solid regions are then defined by whether the shear is large enough to overcome the effec-

tive adhesion and move the rings by a distance greater than the maximal contact length. Therefore, in contrast with rigid granular media where the number of contacts controls the jamming transition [4], the transition with squishy grains in a high friction limit seems to be strongly controlled by the extent of the contacts (Extended Data Fig. 3).

Discussion

We established that large shape deformation may radically modify the mechanisms by which an assembly yields. At high density, far into the jammed state, the number of contacts becomes irrelevant, and their extent, coupled with frictional interactions, becomes crucial. The contact size is intrinsically linked to the geometrical deformations of the elements, so the shape also has a crucial role in the rigidity transition. Geometry and friction concur to generate an attractive force between rings under shear, and sufficient shear must be applied to overcome this effective adhesion. In the high friction limit, the shear must be enough to separate the rings completely to overcome the adhesion; hence, a simple geometric formula (Eq. (1)) sets the transition between repulsive and attractive interactions. Below this transition (when the interactions are attractive), structural rearrangements are strongly hindered, leading to a jammed assembly.

However, these results are valid only within significant friction and shear limits. Our geometrical model implies that a frictionless assembly yields at an infinitesimal shear as $\gamma_r = \mu$. By considering only the interactions between two rings, we neglect collective effects, such as the caging [51], that would require a finite shear to yield even without friction. How caging is affected by significant shape changes is still an open question.

Another striking property of the ring assembly is the drastic structure change between the fluid and solid state. Counterintuitively, the fluid phase features highly crystallised portions, while the solid remains in an amorphous structure. Similarly to the link between active matter and sheared granular media [52], one may also draw a parallel between this fluid-like crystal under shear and active crystals [53, 54].

From an engineering perspective, assemblies of highly deformable elements combine frictional interactions and structural rearrangement to dissipate energy while keeping a significant elastic component [55]. Ring assemblies then have great potential as a tunable shock absorber, with the density serving as a knob to tune dissipation and response to a shock, keeping even a high dissipative potential in the solid and reversible state. To develop this axis, it would be essential to explore the 3D version of such assemblies and their response to inertial forces.

* poincloux@phys.aoyama.ac.jp; Current affiliation: Department of Physical Sciences, Aoyama Gakuin University, 5-10-1 Fuchinobe, Sagamihara, Kanagawa 252-5258, Japan
† kat@kaztake.org

[1] Robert Kostynick, Hadis Matinpour, Shravan Pradeep, Sarah Haber, Alban Sauret, Eckart Meiburg, Thomas Dunne, Paulo Arratia, and Douglas Jerolmack. Rheology of debris flow materials is controlled by the distance from jamming. *Proc. Natl. Acad. Sci. U.S.A.*, 119(44):e2209109119, 2022.

[2] Tianyue Xu, Jianqun Yu, Yajun Yu, and Yang Wang. A modelling and verification approach for soybean seed particles using the discrete element method. *Adv. Powder Technol.*, 29(12):3274–3290, 2018.

[3] Edouard Hannezo and Carl-Philipp Heisenberg. Rigidity transitions in development and disease. *Trends Cell Biol.*, 32(5):433–444, 2022.

[4] Silke Henkes, Martin van Hecke, and Wim van Saarloos. Critical jamming of frictional grains in the generalized isostaticity picture. *Europhys. Lett.*, 90(1):14003, 2010.

[5] Carolina Brito, Harukuni Ikeda, Pierfrancesco Urbani, Matthieu Wyart, and Francesco Zamponi. Universality of jamming of nonspherical particles. *Proc. Natl. Acad. Sci. U.S.A.*, 115(46):11736–11741, 2018.

[6] Jasna Brujić, Chaoming Song, Ping Wang, Christopher Briscoe, Guillaume Marty, and Hernán A. Makse. Measuring the Coordination Number and Entropy of a 3D Jammed Emulsion Packing by Confocal Microscopy. *Phys. Rev. Lett*, 98(24):248001, 2007.

[7] J. Winkelmann, F.F. Dunne, V.J. Langlois, M.E. Möbius, D. Weaire, and S. Hutzler. 2D foams above the jamming transition: Deformation matters. *Colloids Surf. A: Physicochem. Eng. Asp.*, 534:52–57, 2017.

[8] Arman Boromand, Alexandra Signoriello, Janna Lowensohn, Carlos S Orellana, Eric R Weeks, Fangfu Ye, Mark D Shattuck, and Corey S O'Hern. The role of deformability in determining the structural and mechanical properties of bubbles and emulsions. *Soft matter*, 15(29):5854–5865, 2019.

[9] Jonathan Barés, Manuel Cárdenas-Barrantes, David Cantor, Mathieu Renouf, and Émilien Azéma. Softer than soft: Diving into squishy granular matter. *Pap. Phys.*, 14(15):140009–140009, 2022.

[10] Nicoletta Gnan and Emanuela Zaccarelli. The microscopic role of deformation in the dynamics of soft colloids. *Nat. Phys.*, 15(7):683–688, 2019.

[11] Nicoletta Gnan, Fabrizio Camerin, Giovanni Del Monte, Andrea Ninarello, and Emanuela Zaccarelli. Dynamical properties of different models of elastic polymer rings: Confirming the link between deformation and fragility. *J. Chem. Phys.*, 154(15):154901, 2021.

[12] Arman Boromand, Alexandra Signoriello, Fangfu Ye, Corey S. O'Hern, and Mark D. Shattuck. Jamming of Deformable Polygons. *Phys. Rev. Lett*, 121(24):248003, 2018.

[13] Dong Wang, John D. Treado, Arman Boromand, Blake Norwick, Michael P. Murrell, Mark D. Shattuck, and Corey S. O'Hern. The structural, vibrational, and mechanical properties of jammed packings of deformable particles in three dimensions. *Soft Matter*, 17(43):9901–9915, 2021.

[14] Joel T. Clemmer, Joseph M. Monti, and Jeremy B. Lechman. A soft departure from jamming: the compaction of deformable granular matter under high pressures. *Soft Matter*, 20(8):1702–1718, 2024.

[15] Boris Guirao, Stephane U Rigaud, Floris Bosveld, Anaïs Bailles, Jesus Lopez-Gay, Shuji Ishihara, Kaoru Sugimura, François Graner, and Yohanns Bellaïche. Unified quantitative characterization of epithelial tissue development. *eLife*, 4:e08519, 2015.

[16] Dapeng Bi, J. H. Lopez, J. M. Schwarz, and M. Lisa Manning. A density-independent rigidity transition in biological tissues. *Nat. Phys.*, 11(12):1074–1079, 2015.

[17] Jin-Ah Park, Jae Hun Kim, Dapeng Bi, Jennifer A Mitchel, Nader Taheri Qazvini, Kelan Tantisira, Chan Young Park, Maureen McGill, Sae-Hoon Kim, Bomi Gweon, et al. Unjamming and cell shape in the asthmatic airway epithelium. *Nat. Mater.*, 14(10):1040–1048, 2015.

[18] Dapeng Bi, Xingbo Yang, M. Cristina Marchetti, and M. Lisa Manning. Motility-Driven Glass and Jamming Transitions in Biological Tissues. *Phys. Rev. X.*, 6(2):021011, 2016.

[19] Dawa Seo, Changbum Sohn, Mehmet B Cil, and Giuseppe Buscarnera. Evolution of particle morphology and mode of fracture during the oedometric compression of sand. *Géotechnique*, 71(10):853–865, 2021.

[20] Wei Hu, Ching Shung Chang, Mauri McSaveney, Runqiu Huang, Qiang Xu, Yangshuai Zheng, and Jiefu Yu. A weakening rheology of dry granular flows with extensive brittle grain damage in high-speed rotary shear experiments. *Geophys. Res. Lett.*, 47(11):e2020GL087763, 2020.

[21] Y. D. Zhang, G. Buscarnera, and I. Einav. Grain size dependence of yielding in granular soils interpreted using fracture mechanics, breakage mechanics and Weibull statistics. *Géotechnique*, 66(2):149–160, 2016.

[22] Shomeek Mukhopadhyay and Jorge Peixinho. Packings of deformable spheres. *Phys. Rev. E.*, 84(1):011302, 2011.

[23] Jonathan Barés, Manuel Cárdenas-Barrantes, Gustavo Pinzón, Edward Andò, Mathieu Renouf, Gioacchino Viggiani, and Emilien Azéma. Compacting an assembly of soft balls far beyond the jammed state: Insights from three-dimensional imaging. *Phys. Rev. E.*, 108(4):044901, 2023.

[24] M Lisa Manning. Essay: Collections of deformable particles present exciting challenges for soft matter and biological physics. *Phys. Rev. Lett*, 130(13):130002, 2023.

[25] Saeid Nezamabadi, Farhang Radjai, Julien Averseng, and Jean-Yves Delenne. Implicit frictional-contact model for soft particle systems. *J. Mech. Phys. Solids*, 83:72–87, 2015.

[26] Giuseppe Negro, Livio Nicola Carenza, Giuseppe Gonnella, Fraser Mackay, Alexander Morozov, and Davide Marenduzzo. Yield-stress transition in suspensions of deformable droplets. *Sci. Adv.*, 9(22):eadf8106, 2023.

[27] Nen Saito and Shuji Ishihara. Active deformable cells undergo cell shape transition associated with percolation of topological defects. *arXiv:2303.03580*, 2023.

[28] Daan Haver, Daniel Acuña, Shahram Janbaz, Edan Lerner, Gustavo Düring, and Corentin Coulais. Elasticity and rheology of auxetic granular metamaterials. *Proc. Natl. Acad. Sci. U.S.A.*, 121(14):e2317915121, 2024.

[29] Adel Djellouli, Bert Van Raemdonck, Yang Wang,

Yi Yang, Anthony Caillaud, David Weitz, Shmuel Rubinstein, Benjamin Gorissen, and Katia Bertoldi. Shell buckling for programmable metafluids. *Nature*, pages 1–6, 2024, DOI:10.1038/s41586-024-07163-z.

[30] C. Poirier, M. Ammi, D. Bideau, and J. P. Troadec. Experimental study of the geometrical effects in the localization of deformation. *Phys. Rev. Lett*, 68(2):216–219, 1992.

[31] S. D. Papka and S. Kyriakides. Biaxial crushing of honeycombs:—Part 1: Experiments. *Int. J. Solids Struct.*, 36(29):4367–4396, 1999.

[32] Christelle Combescure, Pierre Henry, and Ryan S. Elliott. Post-bifurcation and stability of a finitely strained hexagonal honeycomb subjected to equi-biaxial in-plane loading. *Int. J. Solids Struct.*, 88-89:296–318, 2016.

[33] Chenglin Yang and Stelios Kyriakides. Crushing of low density foams under triaxial loadings. *Extreme Mech. Lett.*, page 11, 2020.

[34] Nathan C. Keim and Paulo E. Arratia. Mechanical and Microscopic Properties of the Reversible Plastic Regime in a 2D Jammed Material. *Phys. Rev. Lett*, 112(2):028302, 2014.

[35] Simon Dagois-Bohy, Ellák Somfai, Brian P. Tighe, and Martin van Hecke. Softening and yielding of soft glassy materials. *Soft Matter*, 13(47):9036–9045, 2017.

[36] Kentaro Nagasawa, Kunimasa Miyazaki, and Takeshi Kawasaki. Classification of the reversible–irreversible transitions in particle trajectories across the jamming transition point. *Soft Matter*, 15(38):7557–7566, 2019.

[37] Pallabi Das, H. A. Vinutha, and Srikanth Sastry. Unified phase diagram of reversible–irreversible, jamming, and yielding transitions in cyclically sheared soft-sphere packings. *Proc. Natl. Acad. Sci. U.S.A.*, 117(19):10203–10209, 2020.

[38] Michio Otsuki and Hisao Hayakawa. Softening and Residual Loss Modulus of Jammed Grains under Oscillatory Shear in an Absorbing State. *Phys. Rev. Lett*, 128(20):208002, 2022.

[39] Zhikun Zeng, Shuyang Zhang, Xu Zheng, Chengjie Xia, Walter Kob, Ye Yuan, and Yujie Wang. Equivalence of Fluctuation-Dissipation and Edwards' Temperature in Cyclically Sheared Granular Systems. *Phys. Rev. Lett*, 129(22):228004, 2022.

[40] Kyu Hyun, Manfred Wilhelm, Christopher O Klein, Kwang Soo Cho, Jung Gun Nam, Kyung Hyun Ahn, Seung Jong Lee, Randy H Ewoldt, and Gareth H McKinley. A review of nonlinear oscillatory shear tests: Analysis and application of large amplitude oscillatory shear (laos). *Prog. Polym. Sci.*, 36(12):1697–1753, 2011.

[41] Daniel Bonn, Morton M Denn, Ludovic Berthier, Thibaut Divoux, and Sébastien Manneville. Yield stress materials in soft condensed matter. *Rev. Mod. Phys.*, 89(3):035005, 2017.

[42] D Richard, Misaki Ozawa, S Patinet, E Stanifer, B Shang, SA Ridout, B Xu, G Zhang, PK Morse, J-L Barrat, et al. Predicting plasticity in disordered solids from structural indicators. *Phys. Rev. Mater.*, 4(11):113609, 2020.

[43] KL Galloway, EG Teich, XG Ma, Ch Kammer, IR Graham, NC Keim, C Reina, DJ Jerolmack, AG Yodh, and PE Arratia. Relationships between structure, memory and flow in sheared disordered materials. *Nat. Phys.*, 18(5):565–570, 2022.

[44] Carl F Schreck, Corey S O'Hern, and Leonardo E Silbert. Tuning jammed frictionless disk packings from isostatic to hyperstatic. *Phys. Rev. E.*, 84(1):011305, 2011.

[45] Andreea Panaitescu, K. Anki Reddy, and Arshad Kudrolli. Nucleation and Crystal Growth in Sheared Granular Sphere Packings. *Phys. Rev. Lett*, 108(10):108001, 2012.

[46] M. Hanifpour, N. Francois, S.M. Vaez Allaei, T. Senden, and M. Saadatfar. Mechanical Characterization of Partially Crystallized Sphere Packings. *Phys. Rev. Lett*, 113(14):148001, 2014.

[47] John R. Royer and Paul M. Chaikin. Precisely cyclic sand: Self-organization of periodically sheared frictional grains. *Proc. Natl. Acad. Sci. U.S.A.*, 112(1):49–53, 2015.

[48] Frank Rietz, Charles Radin, Harry L. Swinney, and Matthias Schröter. Nucleation in Sheared Granular Matter. *Phys. Rev. Lett*, 120(5):055701, 2018.

[49] Sandip Mandal, Maxime Nicolas, and Olivier Pouliquen. Insights into the rheology of cohesive granular media. *Proc. Natl. Acad. Sci. U.S.A.*, 117(15):8366–8373, 2020.

[50] Atsushi Ikeda, Ludovic Berthier, and Peter Sollich. Unified study of glass and jamming rheology in soft particle systems. *Phys. Rev. Lett*, 109(1):018301, 2012.

[51] G. Marty and O. Dauchot. Subdiffusion and Cage Effect in a Sheared Granular Material. *Phys. Rev. Lett*, 94(1):015701, 2005.

[52] Peter K Morse, Sudeshna Roy, Elisabeth Agoritsas, Ethan Stanifer, Eric I Corwin, and M Lisa Manning. A direct link between active matter and sheared granular systems. *Proc. Natl. Acad. Sci. U.S.A.*, 118(18):e2019909118, 2021.

[53] Guillaume Briand, Michael Schindler, and Olivier Dauchot. Spontaneously Flowing Crystal of Self-Propelled Particles. *Phys. Rev. Lett*, 120(20):208001, 2018.

[54] Leonardo Galliano, Michael E. Cates, and Ludovic Berthier. Two-dimensional crystals far from equilibrium. *Phys. Rev. Lett*, 131(4):047101, 2023.

[55] Tomohiko G. Sano, Emile Hohnadel, Toshiyuki Kawata, Thibaut Métivet, and Florence Bertails-Descoubes. Randomly stacked open cylindrical shells as functional mechanical energy absorber. *Commun. Mater.*, 4(1):59, 2023.

Methods

Ring fabrication

Rings are fabricated from silicone elastomer (Elite Double 22, Zhermack) in a urethane mould (Clear Flex 50, Smooth-On). The ring's material is chosen to remain elastic without permanent deformation, even under high and prolonged deformations. The mould material has been selected for its deformability, which eases demoulding without tearing the rings, and its very low affinity with silicone, ensuring no adhesion with the rings and reusability. The rings have a thickness of $t = 1.5\,\text{mm}$, a midline radius $r = 3.3\,\text{mm}$ and height $h = 10\,\text{mm}$. To help with later image analysis, a thin layer ($1\,\text{mm}$) of dyed (Silc Pig Electric Orange, Smooth-On) silicone is applied on the inner portion of the ring surface (from $r - t/2$ to r). This extra layer does not affect the mechanics of the ring (the additional layer is not reproduced

in FEM but still compares well with the experiments, Fig. 1**b,c**). The rings are slightly coated with talc powder to avoid adhesion and ensure reproducible frictional properties. See Supplementary Fig. 1 for an illustration of the protocol.

Shear setup

The shear cell comprises a fixed bottom arm and a movable top arm with movements constrained parallel to the bottom. The two sides of the cell freely rotate respectively to the top and bottom arms via joints of radius 40 mm, and freely slide through the top arm via roller bearings to adjust their length under large oscillatory shear. The distance between the two side arms is $W = 300$ mm, and the one between the top and bottom arm is $T = 75$ mm. Both bottom and top arms are decorated by rigid (3D-printed in PLA and then glued) half disks of radius $r_h = r + t/2 = 4.05$ mm (external radius of the rings). The whole setup rests on a fixed acrylic plate, and the ring assembly is confined vertically by a 3 mm thick acrylic plate blocked in the vertical direction but free to move laterally. The top arm imposes shear via a driving screw controlled by a stepper motor (AZM 46AC-TS10R, Oriental Motor). The motor imposes a cyclic horizontal motion $X = (X_0/2)\sin\left(2\dot{X}_0 t/X_0\right)$, with X_0 the displacement amplitude and $\dot{X}_0 = 1$ mm/s the maximum shear speed, kept constant for all the amplitudes considered. The resulting oscillatory shear is $\gamma = X/T$. The density of the rings is calculated by $\Phi = N\pi r_h{}^2/A$, where $A = 16500$ mm^2 is the area of the shear cell, evaluated by taking into account the size of the joints and the top and bottom granular boundary conditions. With the highest shear considered, this area varies between 16500 mm^2 and 17500 mm^2 within a shear cycle ($\sim 6\%$ of variations). Consequently, densities are defined with uncertainties of $\sim \pm 0.02$. The motor, force sensor, and camera are controlled and synchronised via a custom Labview program.

Force measurements

All forces reported here are measured with a flat six-axis (forces and moments along the three directions) force sensor (USX10-H10-500N-C, TecGihan) and transferred to a computer via 2 data acquisition cards (USB-6001, National Instrument). To measure the shear response of the assembly (Fig. 1**f**), the sensor is inserted between the top arm and the driving screw. The top arm is slightly lifted from the bottom acrylic plate to avoid measuring the frictional response of the setup. All six axes of the sensor are recorded at a rate of 20 Hz. The first harmonic of the loss and storage moduli are computed by $G' = (2/\pi\gamma_0)\int_0^{2\pi} F_y(\theta)\sin\theta \mathrm{d}\theta/WH$ and $G'' = (2/\pi\gamma_0)\int_0^{2\pi} F_y(\theta)\cos\theta \mathrm{d}\theta/WH$ with $\theta = (t - t_c)2\dot{\gamma}_0/\gamma_0$ the normalised time since the start of cycle c [38]. To measure the compression response of the rings (Fig. 1**b,c**) and their interactions (Fig. 4**b,c**), a distinct setup is used where positions are imposed manually via a micrometric

stage and 100 mm long arm levers, and forces are measured via the moments output of the sensor. For the compression response, one free ring is confined between two rigid walls, while for the interaction experiments, a PLA 3D-printed part holding half of the rings into a groove clamps the pair of rings. For one interaction experiment, the six axes of the sensor are recorded continuously at 100 Hz while compression and shear are imposed via manually moving the micrometric stage. The displacement is made by step of 50 μm every 10 s. For every step, the position is changed between 0 and 5 s, and the reported value for this new position is average over the time interval between 7 and 9 s. The arm lever's high but finite stiffness is measured in compression and shear and used to correct the displacement imposed on the rings.

Finite Element Method (FEM)

The mechanical tests using full 3D FEM were performed with the software COMSOL Multiphysics 6.1. We use symmetries to model only the necessary portions of the ring for the compression (Fig. 1**b,c**) and shear (Fig. 4) simulations. The rings are cylinders of height H along the z axis and of external radius r_h in the xy plane. Rings are compressed and sheared in the xy plane, and we assume stress-free surfaces at $z = 0$ and $z = H$. From symmetries, we model only half of the rings, from $z = 0$ to $z = H/2$, with a free surface at $z = 0$ and a mirror symmetry (no outward displacement) at $z = H/2$. The tetrahedral mesh size is fixed and set to a minimum of $\sqrt{rt}/5$, chosen to optimise convergence. The material is the Neo-Hookean model with Young modulus $E = 1$ MPa and Poisson's ratio $\nu = 0.45$. The mechanical tests are performed via a stationary approach and by imposing displacements. For the compression tests (Fig. 1**b,c**), the ring is compressed between two flat and infinitely rigid blocks, and contacts are solved via the Nitsche method. For the interaction tests (Fig. 4), two facing rings are cut again along the x direction to form semi-circles. To clamp the rings, no displacement in the xz plane is imposed on the cut surfaces of the top ring. The position of the bottom ring, first along y for compression and then x for shearing, is also controlled by imposing the displacement of its cut surfaces. The contacts are also solved using the Nitsche method, but this time adding a Coulomb frictional interaction term with a unique friction coefficient μ. The resulting shear force f_x is then obtained by integrating the σ_{yx} component of the stress on the surfaces at $y = 0$ of the bottom ring, where the shear displacement is imposed.

Image acquisition and analysis

Pictures are acquired via a camera (EMVC-CB1400C3 with an EMVL-MP814 lens, Misumi) placed on top of the assembly. Indirect lighting is obtained by shining a light-emitting diode panel on a whiteboard. Irrespective of shear amplitude, 15 pictures per shear cycle are taken (30 pictures for $(\gamma_0, \Phi) = (0.400, 0.94), (0.533, 0.94), (0.533, 1.00)$ where tracking is

more challenging), and a $5\,\mathrm{s}$ pause between the cycles is implemented to ensure that each cycle's first and last pictures correspond to $\gamma = 0$. The pictures consist of 4608×1300 pixels, resulting in a resolution of $13.05\,\mathrm{pixel/mm}$. Then, a custom-made Matlab script processes all the pictures. Using the orange-coloured inner part of the rings, they are detected and separated via colour and saturation thresholding. A group of pixels within its contour is attributed to each detected ring and, for instance, used to represent ring-specific quantities via colour coding, as in Fig. 1**d**. The geometrical centre of the pixels defines then the position of the ring, while its shape, or contour, is measured via a circle Fourier decomposition [27]. The polar coordinates $R(\theta)$ of the outermost pixels of the contour are measured with the geometrical centre of the ring as the origin. Using the fast Fourier transform, the Fourier coefficients (a_k, b_k) of the contour are measured such that

$$R(\theta) = r_h \sum_{k=0}^{M} (a_k \cos\theta + b_k \sin\theta)$$ up to $M = 5$. In addition to the position and shape of the ring, we also detect their neighbours via two methods. First, we find topological neighbours via their position by performing the Delaunay tessellation. Based on the resulting Voronoi diagram, we defined Voronoi neighbours as rings sharing a common edge and no farther than $2.5r$. From this Voronoi neighbourhood, quantities such as the orientational bond order parameter Ψ_6 are computed (see Fig. 2). The other neighbourhood detection method aims to detect the rings in contact. A given ring's contour is dilated by $8\,\mathrm{pixels}$, and its touching neighbours are those whose contour overlaps. Based on these touching rings, we then compute the geometrical and topological strains (Fig. 3**d**,**e**, detailed below) and the contact extents for Fig. 4**e**. To measure the extent of the contacts ℓ_c, we compute the long axis of the overlapping contours. Indeed, each overlap has an approximate ellipsoidal shape with its long axis along the contacting surfaces (see ring overlaps in Extended Data Fig. 2**b**). This measure overestimates the actual contact length because of the dilatation of the central ring, and we found that multiplying by 0.7 gives a visually convincing measure.

Geometrical and topological strains

To distinguish quantitatively the geometrical deformations (change of shape) from the structural or topological ones (change in neighbours), we follow the method introduced in Ref. [15]. Initially developed for epithelial tissue development, this strain quantification can be directly applied to our ring assembly. The method is described in great detail in the Appendix section of Ref. [15], so here, we only give the general methodology and highlight the specificities of our ring assemblies. Strain evaluation is based on the variations of the texture tensor of the assembly computed from the links between each ring. The texture tensor of the assembly is defined as

$\mathbf{M} = \sum_i \frac{1}{2} \sum_{k \sim i} \vec{l}_{ik} \otimes \vec{l}_{ik}$, with $\vec{l}_{ik}$ the vector linking the position of ring i to its neighbour k, i spans all tracked ring of the assembly and k all neighbours of ring i and $\vec{l}_{ik} \otimes \vec{l}_{ik} = \vec{l}_{ik}\vec{l}_{ik}^T$ is the tensor product of $\vec{l}_{ik}$ by itself. In contrast with epithelial tissues, ring assemblies are not confluent, so we must specify what neighbours we consider here. As rings interact only via contact, we consider only touching rings as neighbours to compute the texture tensor. Between two consecutive time frames, the strains are computed from the difference of texture tensor $\mathbf{M}$ between the two frames. The difference within links that are preserved between the two frames will be the base to compute the geometrical strain $\mathbf{S}^*$, while the appearing and disappearing links due to rearrangements only (no fusion or division, unlike in epithelial tissues) will contribute to the topological strain $\mathbf{T}^*$. To make the difference in texture tensor dimensionless and endowed with strain properties, such as insensitivity to rigid motion, a rigorous normalisation detailed in Ref. [15] is necessary. Between two time frames, we can compute two strain tensors, $\mathbf{S}^*$ and $\mathbf{T}^*$, rigorously quantifying the geometrical and topological deformation of the ring assembly. To compare how the assemblies deform during shear cycles as a function of the control parameters (Φ, γ_0), we take the norm of these strain tensors and sum them over the 6 shear cycles in the steady state. The norm is the square root of the sum of the squared elements of the matrices. The resulting quantities, $S_c = \int_t \|\mathbf{S}^*\| \mathrm{d}t$ and $T_c = \int_t \|\mathbf{T}^*\| \mathrm{d}t$, are the scalar quantities shown in Fig. 3**d**,**e**.

Authors contribution.
S.P. and K.A.T. designed the experiments. S.P. performed the experiments, the numerical simulations, the data analysis, and conceived the model. All authors analysed and discussed the results and contributed to writing the paper.

Code and data availability
The Zenodo repository 10.5281/zenodo.10961344, contains the experimental data for the force and from image analysis for ring assemblies and single ring experiments. The raw images of the first five cycles for $\gamma_0 = 0.40$ and $\Phi = 1.00$ and the MATLAB code to process them. It also contains the FEM data and associated COMSOL files.
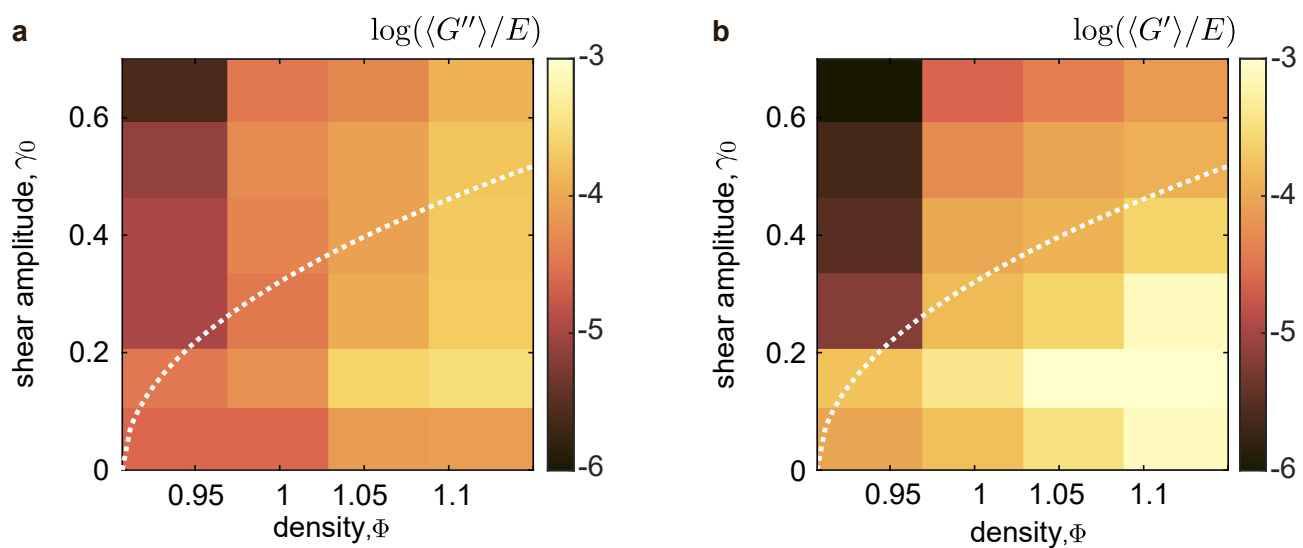
Extended Data Fig. 1 | Loss and storage moduli across the parameter space. The first harmonic of the loss and storage moduli are shown in **a** and **b**, respectively. The moduli are normalised by the Young modulus of the rings, $E = 1\,\text{MPa}$.

a

$$\mathbf{T_n} = T_n(\sin\alpha\,\mathbf{e_x} - \cos\alpha\,\mathbf{e_y})$$

$$\mathbf{T_t} = \mu T_n(-\cos\alpha\,\mathbf{e_x} - \sin\alpha\,\mathbf{e_y})$$

$$\tan\alpha = \frac{x}{2r_h - \delta_y}$$

$$f_x = (\mathbf{T_n} + \mathbf{T_t})\cdot\mathbf{e_x}$$

$$f_x(x = x_r) = 0 \Rightarrow \mu = \tan\alpha = \frac{x_r}{2r_h - \delta_y}$$

$$\Rightarrow x_r = \mu(2r_h - \delta_y)$$

b

$$\left(\tfrac{\ell_c}{2}\right)^2 = r_h^2 + \left(r_h - \tfrac{\delta_y}{2}\right)^2 \Rightarrow x_r = \ell_c = 2r_h\sqrt{1 - \left(1 - \tfrac{\delta_y}{2r_h}\right)^2}$$

c

$$\Phi_h = \frac{3\times(\text{area disk})}{(\text{area hexagon})}$$

$$= \frac{3\times\pi r_h^2}{\frac{3\sqrt{3}}{2}(2r_h)^2} = \frac{\pi}{2\sqrt{3}}$$

$$\Phi = \frac{3\times(\text{area disk})}{(\text{area hexagon})}$$

$$= \frac{3\times\pi r_h^2}{\frac{3\sqrt{3}}{2}(2r_h-\delta_y)^2} = \frac{\Phi_h}{\left(1-\frac{\delta_y}{2r_h}\right)^2}$$

d

$$\gamma = \frac{X}{T} \qquad\qquad \gamma = \frac{x}{2r_h-\delta_y}$$
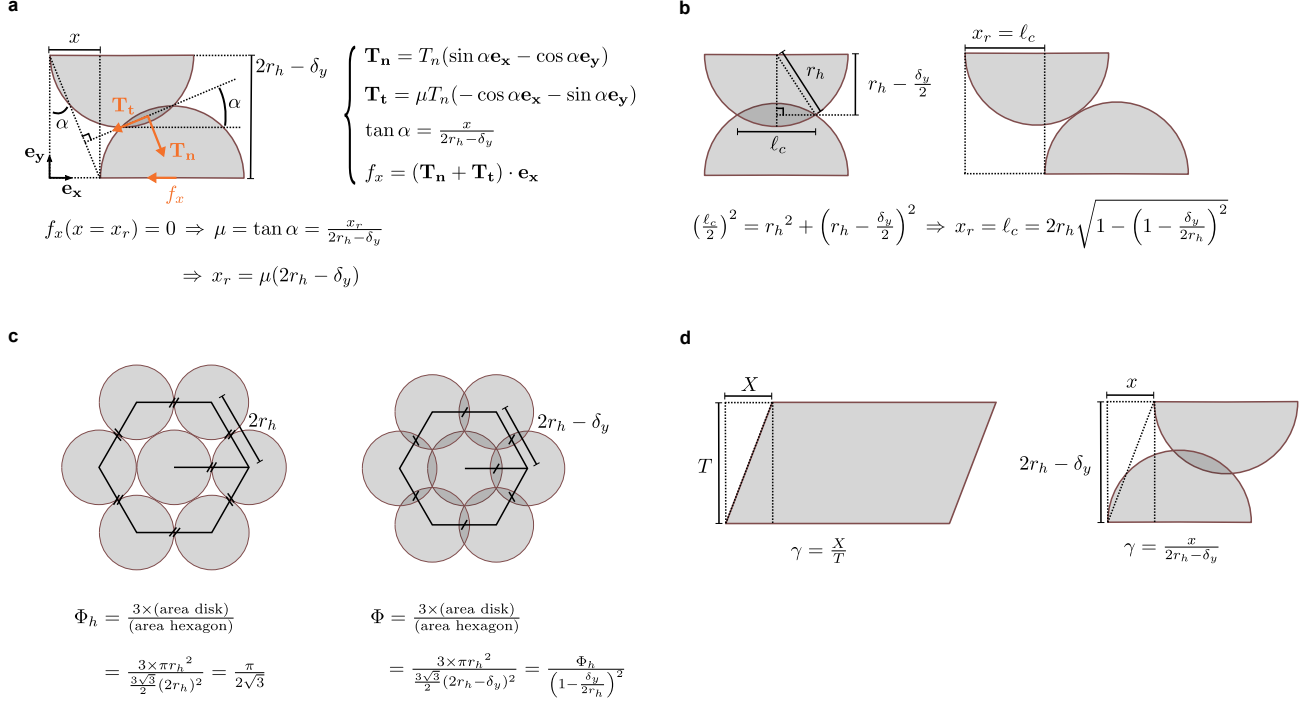
Extended Data Fig. 2 | Schematic for the geometrical predictions. a, First case to estimate the lateral displacement x_r which for which the lateral force f_x becomes repulsive ($f_x > 0$). The contact is reduced to a single point with an orientation α given by the line linking the two intersection points of the half-circles. Assuming frictional Coulomb interactions, the amplitude of tangential $\mathbf{T_t}$ and normal $\mathbf{T_n}$ contact forces are linked by the friction coefficient μ. The lateral force f_x is the resultant of the contact forces projected on the lateral axis: $f_x = (\mathbf{T_n} + \mathbf{T_t})\cdot\mathbf{e_x}$. The expression for x_r is then found by solving the equation $f_x(x = x_r) = 0$. This prediction is valid if the two rings are still in contact at $x = x_r = \mu(2r_r - \delta_y)$. **b**, If the rings are not in contact at $x = x_r = \mu(2r_r - \delta_y)$, we have to consider the second case where f_x remains attractive until complete separation of the rings. In that case, x_r is the no-overlap distance given by the initial contact extent ℓ_c after compression. **c**, To link the global assembly density Φ and the local compression δ_y, we assume an isotropic and homogeneous compression of an assembly initially in a hexagonal packing. The density is estimated by considering a central ring and the hexagon with corners at the centre of its 6 neighbours and by taking the ratio between the area of the ring inside the hexagon (1 full ring + 6 third of rings) and the area of the hexagon. In the hexagonal lattice, the hexagon edge is $2r_h$ and reduces to $2r_h - \delta_y$ under compression, while the area of the rings is constant (Φ is estimated from the area of undeformed rings). **d**, Shear is a scaleless quantity defined as the ratio between the lateral displacement and the height of the system. The shear defined for the assembly as $\gamma_= X/T$ is then identical to the one in the local interaction experiments, $\gamma = x/(2r_h - \delta_y)$.
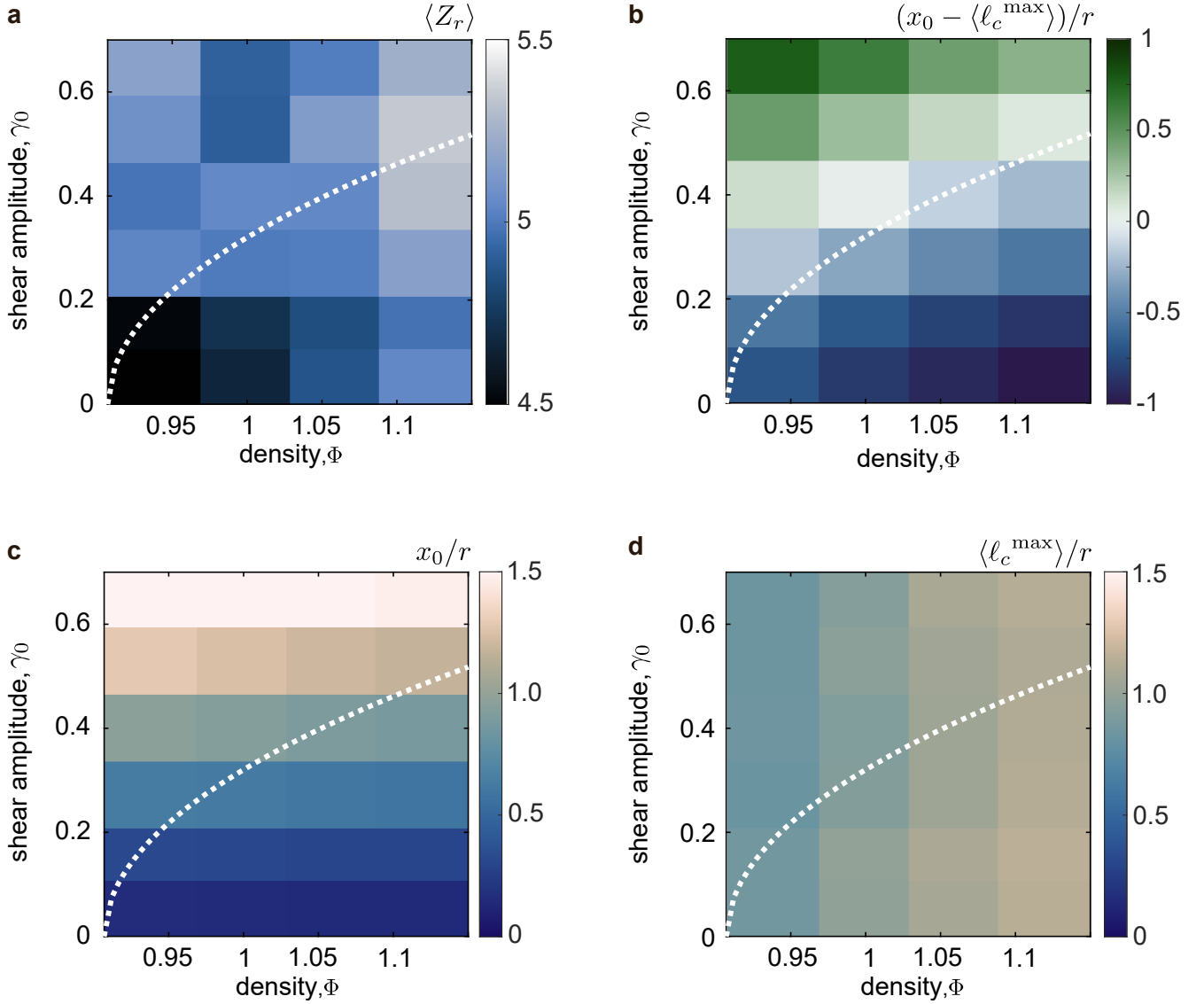
Extended Data Fig. 3 | The average coordination number is irrelevant for highly compressed assemblies. a, Average of the coordination number Z_r of the assemblies in the steady state. The coordination number of a ring is defined as the number of touching neighbours. No clear tendency with γ_0, Φ, or the fluid/solid regions is noticeable. **b**, Reproduction of Fig. 4**e**, showing that the relative value between the shear distance x_0 and the averaged maximal contact length $\langle \ell_c^{\max} \rangle$ marks a clear separation between fluid and solid-like regions. **c**, local average lateral displacement x_0 imposed to the assembly over the parameter space (γ_0, Φ). It is a deterministic quantity computed following $x_0 = \gamma_0 2 r_h \sqrt{\Phi_h / \Phi}$. **d**, For each tracked ring in the steady state, the contact length ℓ_c with each of its touching neighbours is measured (see Methods). At each time-step, the highest ℓ_c of each ring is averaged over all rings, and then all time-steps to give $\langle \ell_c^{\max} \rangle$. While x_0 mainly increases with the shear γ_0, $\langle \ell_c^{\max} \rangle$ is increasing with density Φ. The two values coincide around the fluid-solid separation line predicted by $\gamma_r(\Phi) = \sqrt{\Phi / \Phi_h - 1}$.

Supplementary Material for "Squish Jamming"

Samuel Poincloux[*]

Department of Physics, The University of Tokyo, 7-3-1 Hongo, Bunkyo-ku, Tokyo 113-0033, Japan

Kazumasa A. Takeuchi[†]

Department of Physics, The University of Tokyo,
7-3-1 Hongo, Bunkyo-ku, Tokyo 113-0033, Japan and
Institute for Physics of Intelligence, The University of Tokyo, 7-3-1 Hongo, Bunkyo-ku, Tokyo 113-0033, Japan

(Dated: April 16, 2024)

VIDEO CAPTIONS

Supplementary Video 1: Video of the first ten shear cycles for the assemblies with $(\gamma_0, \Phi) = (0.4, 0.94)$ (top) and $(\gamma_0, \Phi) = (0.4, 1.16)$ (bottom).

Supplementary Video 2: Illustration of the measurements made on the rings, here shown for a single ring and parameters $(\gamma_0, \Phi) = (0.4, 1.0)$. The shape is highlighted in red, and the Voronoi diagram is in fine white dotted lines. Each touching ring and its corresponding bond vector is white, while the contact width is blue.

Supplementary Video 3: Non-affine trajectories of the rings in the steady state. The affine displacement due to the instantaneous shear strain is retrieved for each ring trajectory and time frame along shear cycles.

Supplementary Video 4: An animated version of Fig.2**a,b** showing the probability distribution of Ψ_6 with the number of shear cycles.

Supplementary Video 5: Stroboscopic evolution of the structure of the assemblies with the number of shear cycles. The video shows, for all the experiments, snapshots of the assembly at the start of each cycle with each tracked ring coloured by its Ψ_6 value. The assembly is darkened when it reaches its maximal cycling number.

Supplementary Video 6: Bond vector dynamics of the assemblies. The video shows, for all the experiments, snapshots of the assembly upon cycling in the steady state. For each picture, the links that are conserved are coloured in white, the ones disappearing at the next frame in blue, and the ones appearing from the previous frame in red.

Supplementary Video 7: Video showing the FEM simulation of ring-ring experiments, with snapshots of the rings on the left, and the corresponding shear force $f_x(x)$ in the right. The results for $\mu = 0.3$ and $\mu = 0.6$ are shown for a compression of $\delta_y = 950\,\mu m$.

SUPPLEMENTARY TABLES AND FIGURES

---

[*] poincloux@phys.aoyama.ac.jp
[†] kat@kaztake.org
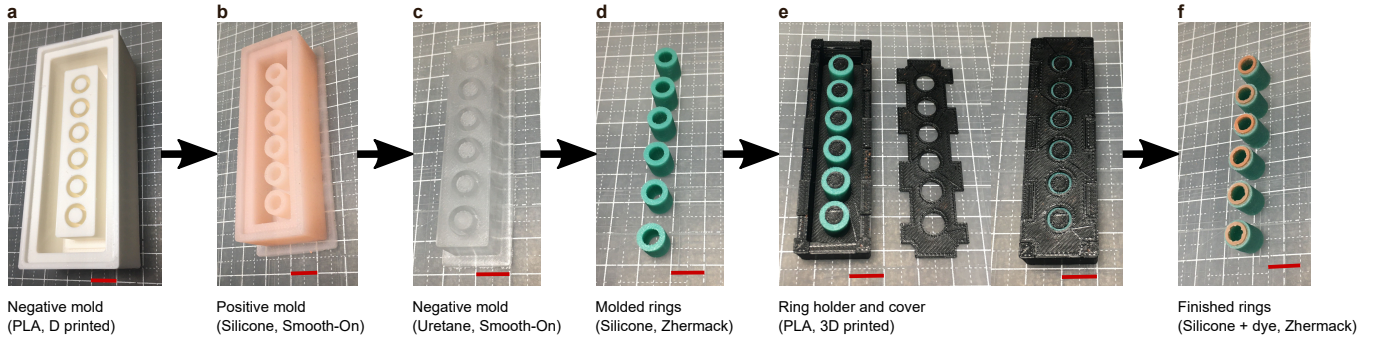
Supplementary Fig. 1 | Fabrication process of the rings. A negative mould 3D printed with PLA (**a**) is used to fabricate a positive mould made of silicone (**b**). The silicone mould itself is used to fabricate a urethane negative mould (**c**), in which the rings are made (**d**). Then, the rings are placed in a 3D printed holder with a cover (**e**), leaving only the internal half of the ring top surface visible. A thin layer of dyed silicone is then coated on the surface to give the final rings (**f**). Before experiments, the rings are placed in a sealed plastic bag with talc powder and thoroughly shaken to ensure a homogeneous coating of the rings. The multiple moulds were used to satisfy the following constraints: the mould needs to be flexible to ensure demoulding without breaking the rings, silicone sticks to silicone moulds, but not at all with urethane (also a soft polymer), urethane sticks to everything except silicone. Only the choice of the silicone for the rings and its coloured top is crucial (Elite Double 22, Zhermack) to ensure no plastic deformation of the rings, even under prolonged and high deformations. The red scale bar in the pictures measures 10 mm.

$\gamma_0 = 0.667$ $(X_0 = 50\,\text{mm})$	$N_c = 100$ $R_{\text{tracked}} = 84.8\%$	$N_c = 15$ $R_{\text{tracked}} = 91.2\%$	$N_c = 15$ $R_{\text{tracked}} = 95.9\%$	$N_c = 15$ $R_{\text{tracked}} = 96.7\%$
$\gamma_0 = 0.533$ $(X_0 = 40\,\text{mm})$	$N_c = 100$ $R_{\text{tracked}} = 92.9\%$	$N_c = 50$ $R_{\text{tracked}} = 95.9\%$	$N_c = 40$ $R_{\text{tracked}} = 97.4\%$	$N_c = 45$ $R_{\text{tracked}} = 97.5\%$
$\gamma_0 = 0.400$ $(X_0 = 30\,\text{mm})$	$N_c = 100$ $R_{\text{tracked}} = 98.3\%$	$N_c = 100$ $R_{\text{tracked}} = 98.7\%$	$N_c = 60$ $R_{\text{tracked}} = 99.1\%$	$N_c = 75$ $R_{\text{tracked}} = 95.3\%$
$\gamma_0 = 0.267$ $(X_0 = 20\,\text{mm})$	$N_c = 100$ $R_{\text{tracked}} = 99.3\%$	$N_c = 100$ $R_{\text{tracked}} = 98.4\%$	$N_c = 100$ $R_{\text{tracked}} = 100\%$	$N_c = 100$ $R_{\text{tracked}} = 99.7\%$
$\gamma_0 = 0.133$ $(X_0 = 10\,\text{mm})$	$N_c = 100$ $R_{\text{tracked}} = 100\%$	$N_c = 100$ $R_{\text{tracked}} = 100\%$	$N_c = 100$ $R_{\text{tracked}} = 99.4\%$	$N_c = 100$ $R_{\text{tracked}} = 99.2\%$
$\gamma_0 = 0.067$ $(X_0 = 5\,\text{mm})$	$N_c = 100$ $R_{\text{tracked}} = 99.7\%$	$N_c = 100$ $R_{\text{tracked}} = 99.7\%$	$N_c = 100$ $R_{\text{tracked}} = 100\%$	$N_c = 100$ $R_{\text{tracked}} = 100\%$
	$\Phi = 0.94$ $(N = 296)$	$\Phi = 1.00$ $(N = 320)$	$\Phi = 1.06$ $(N = 340)$	$\Phi = 1.12$ $(N = 360)$

Supplementary Table 1 | Experimental parameters for the shear experiments. The shear amplitude γ_0 is set by the lateral displacement amplitude of the top arm, X_0, while the density Φ is controlled by the number of rings N. For each set of the parameters (γ_0, Φ), the total number of cycles N_c (including the transient and the steady state) and the proportion of rings successfully tracked R_{tracked} are indicated. The last 6 available cycles (for instance, from cycle 45 to 50 if $N_c = 50$) are considered to be in the steady state and are used for the analyses presented in this work. For instance, for the parameter $(\gamma_0, \Phi) = (0.400, 1.06)$, the measures are made on the cycle $[55, 56, 57, 58, 59, 60]$. Progressive and out-of-plane extrusion of some rings limits the number of valid cycles for high shear and density. Due to the extreme deformability of the rings, upon cycling, some rings manage to escape the plane of the assembly despite the cover plate by out-of-plane deformations. In Supplementary Fig. 2, we verify that the results and following conclusions are not dependent on which cycles we consider as the steady state and make the measurements.
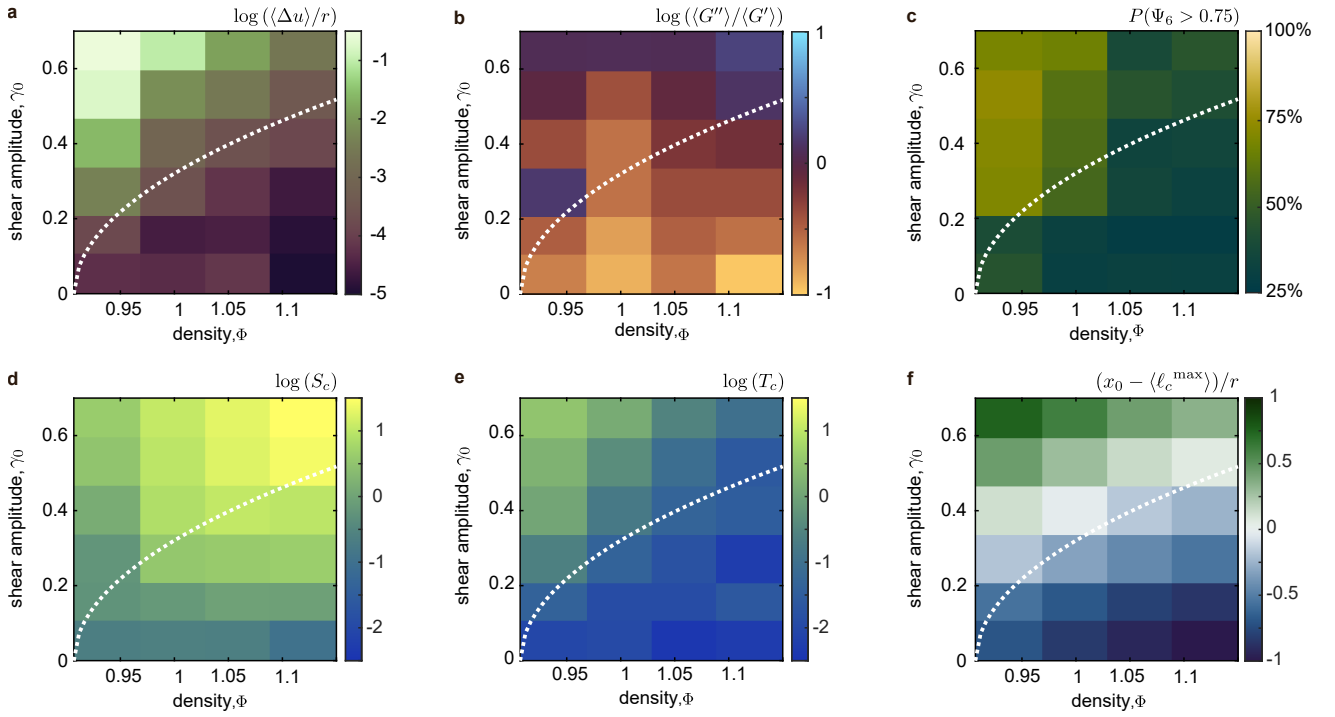
Supplementary Fig. 2 | The quantities in the (γ_0, Φ) parameter space are not sensitive to the definition of the steady state. The parameters map presented in the main figures are reproduced here, for the cycle numbers fixed to be 10 to 15 for all the parameters, the highest numbers common to all parameters. **a,** Irreversible displacement. **b,** Ratio between the viscous and elastic moduli. **c,** Proportion of rings in a crystal cluster. **d,** Geometrical strain. **e,** Topological strain. **f,** Difference between the imposed lateral displacement and maximum contact length. While some quantitative differences can be observed in the proportion of crystal (**c**) and shear moduli (**b**), conveying that the steady state may not be fully settled for the cycle numbers chosen here, the tendency and evolution remain essentially the same. The choice of the cycles to take into account is then not a determining factor in analysing the response of ring assemblies.